

Mathematical modeling and numerical multigoal-oriented a posteriori error control and adaptivity for a stationary, nonlinear, coupled flow temperature model with temperature dependent density

S. Beuchler^{1,3}, A. Demircan^{2,3}, B. Endtmayer^{1,3}, U. Morgner^{2,3}, and T. Wick^{1,3}

¹Cluster of Excellence PhoenixD (Photonics, Optics, and Engineering – Innovation Across Disciplines), Leibniz Universität Hannover, Germany

²Leibniz Universität Hannover, Institute of Quantum Optics, Welfengarten 1, 30167 Hannover, Germany

³ Leibniz Universität Hannover, Institute of Applied Mathematics , Welfengarten 1, 30167 Hannover, Germany

Abstract

In this work, we develop adaptive schemes using goal-oriented error control for a highly nonlinear flow temperature model with temperature dependent density. The dual-weighted residual method for computing error indicators to steer mesh refinement and solver control is employed. The error indicators are used to employ adaptive algorithms, which are substantiated with several numerical tests. Therein, error reductions and effectivity indices are consulted to establish the robustness and efficiency of our framework.

Keywords: Nonlinear PDEs; Navier-Stokes; multigoal error estimation; dual-weighted residual method; adaptivity; finite elements

1 Introduction

This work is devoted to the development of a mathematical model of the Navier-Stokes equations coupled to a heat equation with temperature dependent viscosity and density. The time dependent Navier-Stokes equations with density were investigated in [29], while stationary Navier-Stokes equations with variable density (without temperature) were considered in [35]. Well-known are so-called Boussinesq approximations [48, 34]. The resulting

problem is a highly nonlinear coupled PDE (partial differential equations) system. Applications of temperature dependent viscosities and densities range from ionic liquids [33] over laser material processing [37] up to wave guide modeling [40, 15]. Related theoretical work is [28] in which long-time and large-data existence of a weak solutions were obtained with the viscosity and heat-conductivity coefficients varying with the temperature.

Moreover, nonstationary Navier-Stokes with variable densities and variable viscosities were considered in [38]. Finally, [41] proposed a computational algorithm for the evolutionary Navier-Stokes-Fourier system with temperature dependent material properties such as density, viscosity and thermal conductivity. To the best of our knowledge, exactly our proposed model and numerical realization has not yet been utilized in the literature.

Often in numerical simulations, not the entire numerical solution is of interest, but certain quantities of interest (QoI). Accurate evaluations are obtained with the help of goal-oriented error control with the dual-weighted residual method (DWR) [11] (see also [2, 8, 36]), which serve as basis for mesh adaptivity and balancing discretization and nonlinear iteration errors. The latter ensures that solver tolerances are automatically adjusted according to the current discretization accuracy of the QoIs. As we have a multiphysics situation at hand, multiple QoIs might be of interest simultaneously. This is addressed by multigoal-oriented error control using again the DWR method. Early work was carried out in [31]. Significant improvements from the algorithmic and theoretical level were done by us

in prior work, namely a partition-of-unity localization (based on [44]) for multigoal-oriented error control in [27], balancing discretization and nonlinear iteration errors for multigoal in [23], efficiency and reliability estimates for goal-oriented error control using a saturation assumption in [24], and smart algorithms switching between solving high-order problems or using interpolations in [25]. Additionally, efficiency and reliability estimates for arbitrary interpolations are established in [25].

Other conceptual improvements in multigoal error estimation were done in [45, 39, 13]. Recent applications in stationary multiphysics problems were undertaken in fluid-structure interaction [1] and the Boussinesq equations [12].

The objective in this work is a nontrivial extension of [12] by making the density variable. This results into both temperature-dependent densities and viscosities. Their respective relationships are described with exponential laws. The resulting coupled problem is highly nonlinear. The numerical solution algorithms are based on monolithic formulations in which the entire system is solved all-at-once. Therein, a Newton solver is utilized for the nonlinear solution in which the Newton tolerances are chosen according to the current accuracy of the quantities of interest, i.e., balancing discretization and nonlinear iteration errors. This is achieved by a multigoal-oriented a posteriori error estimates with adjoint problems, using the DWR method,

and was for multigoal error estimation first formulated in [23]. The adjoint needs to be explicitly derived for our coupled problem. In order to utilize the error estimators for local mesh adaptivity, the error needs to be localized, which is here done with a partition-of-unity (PU), proposed for DWR in [44]. These developments result into our final adaptive algorithms. Our numerical examples are inspired from applications in laser material processing.

The outline of this paper is as follows: In Section 2 our model problem and discretization with the Galerkin finite element method are introduced. Next, in Section 3 our goal-oriented framework is introduced. Section 4 is the main part of this paper. Several numerical examples are conducted and investigated with respect to error reductions and effectivity indices. In most of the experiments point-like sources of the heat equation is chosen. The coarse mesh of the approximation requires some a-priori refinement which is explained in Subsection 4.1. This sections contains also comparisons of the simpler model investigated in [12] with the new one. Also computations on a non-polygonal geometry are presented. Finally, our work is summarized in Section 5.

2 The model problem and discretization

2.1 The model problem

Let $\Omega \subset \mathbb{R}^d$, with $d \in \{2, 3\}$, be a bounded Lipschitz domain. As model problem, we consider the Navier-Stokes equation with temperature dependent viscosity and density. The corresponding problem looks as follows: Find the velocity field v , the pressure p and the temperature θ such that

$$\begin{aligned} -\operatorname{div}(\nu(\theta)\rho(\theta)(\nabla v + \nabla v^T)) + (\rho(\theta)v \cdot \nabla)v - \nabla p - g\rho(\theta) &= 0, \\ -\operatorname{div}(\rho(\theta)v) &= 0, \\ -\operatorname{div}(k\nabla\theta) + v \cdot \nabla\theta &= f_E, \\ \rho(\theta) &= \rho_0 e^{-\int_{\theta_0}^{\theta} \alpha(\hat{\theta}) \, d\hat{\theta}}, \\ \nu(\theta) &= \nu_0 e^{\frac{E_A}{R\theta}}, \end{aligned}$$

in Ω . In this paper, we use Dirichlet boundary conditions for velocities and temperature only. More precisely

$$\begin{aligned} v &= 0 && \text{on } \partial\Omega, \\ \theta &= \theta_0 && \text{on } \partial\Omega, \end{aligned}$$

where $k > 0$ is the thermal conductivity and $\theta_0 > 0$. Of course the conditions $v = 0$ on $\partial\Omega$ and $\theta = \theta_0$ on $\partial\Omega$ have to be understood as traces. However, also other boundary conditions do not restrict the result of this work. The viscosity $\nu(\theta)$ is modeled by the Arrhenius equation; see [7, 6] for chemical

reactions and [17, 42, 3, 47, 30] for viscosity. Here, the parameters E_A and ν_0 are material parameters and $R = 8.31446261815324$ is the universal gas constant. The equation for the density is derived from the volume equations in [18], i.e.

$$V(\theta) = V_0 e^{\int_{\theta_0}^{\theta} \alpha(\hat{\theta}) d\hat{\theta}}.$$

Since the density depends on the temperature, the part $g\rho(\theta)$ is not necessarily a gradient field and therefore might change the flow. For constant density, this term just influences the pressure. Furthermore let

$$V_{v,0} := [H_0^1(\Omega)]^d, \quad V_p := L_0^2(\Omega), \quad \text{and} \quad V_{\theta,0} := H_0^1(\Omega).$$

For our model problem, we use the following weak form:

Problem 2.1. Find $U := (v, p, \theta) \in \{0, 0, \theta_0\} + \{V_{v,0} \times V_p \times V_{\theta,0}\} =: U^D + V$ such that

$$\begin{aligned} & (\nu(\theta)\rho(\theta)(\nabla v + \nabla v^T), \nabla \psi_v) + (\rho(\theta)\nabla v \cdot v, \psi_v) + (p, \operatorname{div}(\psi_v)) - (\rho(\theta)g, \psi_v) \\ & + (\operatorname{div}(v)\rho(\theta) - \rho'(\theta)\nabla\theta \cdot v, \psi_p) \\ & + (k\nabla\theta, \nabla\psi_\theta) + (v \cdot \nabla\theta, \psi_\theta) - (f_E, \psi_\theta) = 0 \end{aligned} \tag{1}$$

holds for all $\Psi := (\psi_v, \psi_p, \psi_\theta) \in V$. Additionally, we note that the temperature θ has to be positive. As usual, we reformulate the weak form (1) as the operator equation

$$A(U) = 0 \quad \text{in } V^*,$$

where V^* denotes the dual space of V .

2.2 Discretization and numerical solution

For the discretization, we decompose our domain into hypercubal elements $K \in \mathcal{T}_h$, where $\bigcup_{K \in \mathcal{T}_h} \overline{K} = \overline{\Omega}$ and for all $K, K' \in \mathcal{T}_h$: $K \cap K' = \emptyset$ if and only if $K \neq K'$. Let $\mathbb{Q}_k(K)$ be the tensor product space of polynomials of degree k on the reference domain \hat{K} and

$$Q_k := \{v_h \in \mathcal{C}(\Omega) : \psi_h \in \mathbb{Q}_k(K) \quad \forall K \in \mathcal{T}_h\},$$

the finite element space of continuous finite elements of degree k on \mathcal{T}_h . This leads the usual standard continuous tensor product finite elements on hypercubes. Finally we consider our finite element space for the model problem as $V_h := Q_k^d \times Q_m \times Q_n$. Finally the discretized model problem is given by: Find $U_h := (v_h, p_h, \theta_h) \in U^D + V_h$ such that

$$A(U_h)(\Psi_h) = 0, \tag{2}$$

for all $\Psi_h \in V_h$. In the numerical experiments, we use Q_2 finite elements for the velocity and Q_1 finite elements for the pressure and temperature. Later,

we require an enriched space as in [27]. For the enriched spaces, which will be introduced in the following section, we use Q_4 for the velocity and Q_2 for pressure and temperature. Once a basis is chosen this leads to a system of nonlinear equations. Here, we use Newton's method to solve these arising systems.

3 Goal oriented error estimation with the dual-weighted residual method

Let $U \in U^D + V$ be the solution of our model problem (1). The solution U might not be of primary interest, but in one functional evaluation $J : U^D + V \mapsto \mathbb{R}$ or even several functional evaluations J_1, \dots, J_N evaluated at U . Of course, if we know U , then we can compute these values. However, in general, we get the discrete solution $U_h \in U^D + V_h$ instead of U , which introduces an error in the functional or functionals. To be precise, in many cases we do not even acquire U_h since our model problem is non-linear, but some approximation \tilde{U} of U_h . To estimate the error, i.e $J(U) - J(U_h)$, we use the dual weighted residual (DWR) method [11, 10, 43].

3.1 Single goal

In this subsection, we derive the error estimation for one goal functional J .

The classical approach

First of all, we introduce the adjoint problem: Find $Z := (z_v, z_p, z_\theta) \in V$ such that

$$A'(U)(\Psi, Z) = J'(U)(\Psi), \quad \forall \Psi \in V, \quad (3)$$

and for U as a solution to the model problem (1). Here, $A'(U)$ and $J'(U)$ describe the Fréchet-derivatives of A and J , respectively. The adjoint problem is linear, even if the model problem is highly nonlinear. However, finding Z still requires us to solve a partial differential equation. Discretizing in the same way as for our model problem leads to the discretized adjoint problem: Find $Z_h \in V_h$ such that

$$A'(U_h)(\Psi_h, Z_h) = J'(U_h)(\Psi_h), \quad \forall \Psi_h \in V_h$$

and for U_h as a solution to the discretized model problem (2).

Theorem 3.1 (Error representation(see [43, 23, 20])). *Let $\tilde{Z} \in V_h$ be an approximation to Z_h and $\tilde{U} \in U^D + V_h$ be an approximation to U_h . Furthermore let U be the solution to the model problem (1) and Z be the solution to the adjoint problem (3). Additionally let $A \in \mathcal{C}^3$ and $J \in \mathcal{C}^3$. Then, we have*

the following error identity

$$J(U) - J(\tilde{U}) = \frac{1}{2} \left(\eta_p(\tilde{U})(Z - \tilde{Z}) + \eta_a(\tilde{U}, \tilde{Z})(U - \tilde{U}) \right) + \eta_k(\tilde{U})(\tilde{Z}) + \mathcal{R}^{(3)}, \quad (4)$$

with

$$\eta_p(\tilde{U})(\cdot) := -A(\tilde{U})(\cdot), \quad (5)$$

$$\eta_a(\tilde{U}, \tilde{Z}) := J'(\tilde{U})(\cdot) - A'(\tilde{U})(\cdot, \tilde{Z}), \quad (6)$$

$$\eta_k(\tilde{U})(\tilde{Z}) := -A(\tilde{U})(\tilde{Z}), \quad (7)$$

and $\mathcal{R}^{(3)}$ as higher order term. For more information on $\mathcal{R}^{(3)}$, we refer to [24, 19].

Proof. For the proof we refer to [43, 23, 20]. \square

Usually, the values $U - \tilde{U}$ and $Z - \tilde{Z}$ are not available. It is possible to approximate these quantities by using interpolation techniques [11, 8, 43, 25], or hierarchical approaches (by higher order finite elements or a finer mesh) as done in [11, 8, 44, 9, 14, 46]. A comparison between higher order finite elements and a finer mesh for the Navier-Stokes equation is provided in [22].

An approach on discrete spaces

Here, we introduce an enriched space $V_h^{(2)}$ with $V_h \subset V_h^{(2)} \subset V$ as it is done in the hierarchical approaches above. We introduce the enriched model problem: Find $U_h^{(2)} \in U^D + V_h^{(2)}$ such that

$$A(U_h^{(2)}) = 0 \quad \text{in } V_h^{(2),*}, \quad (8)$$

where $V_h^{(2),*}$ is the dual space of $V_h^{(2)}$. Moreover, the enriched adjoint problem is given by: Find $Z_h^{(2)} \in V_h^{(2)}$ such that

$$A'(U_h^{(2)})(\Psi_h^{(2)}, Z_h^{(2)}) = J'(U_h^{(2)})(\Psi_h^{(2)}), \quad \forall \Psi_h^{(2)} \in V_h^{(2)}, \quad (9)$$

with $U_h^{(2)}$ as the solution of the enriched model problem (8).

Assumption 1 (Saturation assumption; see [24, 26]). Let $U_h^{(2)}$ be the solution of (8). Furthermore, let \tilde{U} be an approximation to (1). Then there is a constant $b_0 \in (0, 1)$ and a constant $b_h \in (0, b_0)$ such that

$$|J(U) - J(U_h^{(2)})| < b_h |J(U) - J(\tilde{U})|.$$

Corollary 3.2. *Let $A : U^D + V \mapsto V^*$ and $J : \mathcal{D}(J) \mapsto \mathbb{R}$. Furthermore, let us assume that $U \in \mathcal{D}(J)$, where U solves the model problem (1). Moreover, we assume that the operator A and the functional J are at least three times Fréchet differentiable on the discrete space $U^D + V_h^{(2)}$. In addition, let $U_h^{(2)} \in U^D + V_h^{(2)}$ be the solution of the enriched model problem (8) and $Z_h^{(2)} \in V_h^{(2)}$ be the enriched adjoint solution (9). Then for arbitrary $\tilde{U} \in U^D + V_h^{(2)}$, $\tilde{Z} \in V_h^{(2)}$ it holds,*

$$J(U) - J(\tilde{U}) = J(U) - J(U_h^{(2)}) + \frac{1}{2} \left(\eta_p(\tilde{U})(Z_h^{(2)} - \tilde{Z}) + \eta_a(\tilde{U}, \tilde{Z})(U_h^{(2)} - \tilde{U}) \right) + \eta_k(\tilde{U})(\tilde{Z}) + \mathcal{R}_h^{(3),(2)},$$

where $\mathcal{R}_h^{(3),(2)}$ is a higher order term in $\left(\|Z_h^{(2)} - \tilde{Z}\| + \|U_h^{(2)} - \tilde{U}\| \right)$ and η_a, η_p and η_k are defined by (5), (6) and (7) as in Theorem 3.1.

Proof. The assertion follows immediately from Corollary 4.4 in [26]. \square

Remark 3.3. *By replacing U by $U_h^{(2)}$ in η_a, η_p and η_k in Theorem 3.1, we observe that they coincide with η_a, η_p and η_k in Corollary 3.2. However, in contrast to Theorem 3.1, it is not required that A and J are three times Fréchet differentiable on the continuous level. In addition, the existence of the adjoint solution is not required anymore. However, the existence of the enriched adjoint solution is required instead. Additionally we need the existence of the functional value $J(U)$.*

Definition 3.4 (Efficient and reliable error estimator for J). *The error estimator η is efficient, if there exists a constant $\underline{c} \in \mathbb{R}$ with $\underline{c} > 0$ such that*

$$\underline{c}|\eta| \leq |J(U) - J(\tilde{U})|.$$

We say an error estimator η is reliable, if there exists a constant $\bar{c} \in \mathbb{R}$ with $\bar{c} > 0$ such that

$$\bar{c}|\eta| \geq |J(U) - J(\tilde{U})|.$$

Definition 3.5. *Following the result of Corollary 3.2, we define our error estimator as*

$$\eta := \frac{1}{2} \overbrace{\left(\eta_p(\tilde{U})(Z_h^{(2)} - \tilde{Z}) + \eta_a(\tilde{U}, \tilde{Z})(U_h^{(2)} - \tilde{U}) \right)}{:=\eta_h} + \eta_k(\tilde{U})(\tilde{Z}) + \mathcal{R}_h^{(3),(2)}.$$

In the work [24] was shown, that the part $\mathcal{R}_h^{(3),(2)}$ indeed is of higher order and therefore can be neglected. The part $\eta_k(\tilde{U})(\tilde{Z})$ can be used to stop the nonlinear solver as suggested in [43, 24]. The following theorem shows efficiency and reliability for the resulting error estimator.

Corollary 3.6 (Efficiency and reliability for η). *Let us assume that Assumption 1 is fulfilled. Furthermore let all assumption of Corollary 3.2 be fulfilled. Then the error estimator η is efficient and reliable with the constants $\bar{c} = \frac{1}{1-b_h}$ and $\underline{c} = \frac{1}{1+b_h}$.*

Proof. The proof follows the same ideas as the proof in [24]. From Corollary 3.2 we know that

$$|J(U) - J(\tilde{U})| = |J(U) - J(U_h^{(2)}) + \eta|.$$

Using the triangle inequality and inverse triangle inequality $|x+y| \geq |x| - |y|$ for $x, y \in \mathbb{R}$, we immediately get

$$|J(U) - J(\tilde{U})| \leq |J(U) - J(U_h^{(2)})| + |\eta| \leq b_h |J(U) - J(\tilde{U})| + |\eta|,$$

and

$$|J(U) - J(\tilde{U})| \geq -|J(U) - J(U_h^{(2)})| + |\eta| \geq -b_h |J(U) - J(\tilde{U})| + |\eta|.$$

This implies that

$$(1 - b_h) |J(U) - J(\tilde{U})| \leq |\eta| \leq (1 + b_h) |J(U) - J(\tilde{U})|.$$

This inequality is equivalent to

$$\frac{1}{1 + b_h} |\eta| \leq |J(U) - J(\tilde{U})| \leq \frac{1}{1 - b_h} |\eta|.$$

□

As localization for the discretization error estimator η_h , we use the partition of unity (PU) technique proposed in [44]. Here, we use the Q_1 finite elements as partition of unity. Let $\Phi_i \in Q_1$. Then, we know that $\sum_{i=1}^{|Q_1|} \Phi_i = 1$. Of course,

$$\frac{1}{2} \left(\eta_p(\tilde{U})(Z_h^{(2)} - \tilde{Z}) + \eta_a(\tilde{U}, \tilde{Z})(U_h^{(2)} - \tilde{U}) \right),$$

is equal to

$$\begin{aligned} & \frac{1}{2} \left(\eta_p(\tilde{U}) \left((Z_h^{(2)} - \tilde{Z}) \sum_{i=1}^{|Q_1|} \Phi_i \right) + \eta_a(\tilde{U}, \tilde{Z}) \left((U_h^{(2)} - \tilde{U}) \sum_{i=1}^{|Q_1|} \Phi_i \right) \right) \\ &= \sum_{i=1}^{|Q_1|} \frac{1}{2} \underbrace{\left(\eta_p(\tilde{U}) \left((Z_h^{(2)} - \tilde{Z}) \Phi_i \right) + \eta_a(\tilde{U}, \tilde{Z}) \left((U_h^{(2)} - \tilde{U}) \Phi_i \right) \right)}_{:= \eta_i^{PU}}. \end{aligned} \quad (10)$$

These η_i^{PU} represent an error distribution of the partition of unity or their corresponding nodes respectively. This nodal error is distributed equally to all elements sharing this node. For more information about this, we refer to [23, 24]. Finally, we want to show efficiency and reliability for η_h using an additional assumption.

Corollary 3.7 (see [21]). *Let us assume that all assumptions of Corollary 3.6 are fulfilled and that there exist a constant $\xi \in (0, 1)$ such that*

$$|\eta_k + \mathcal{R}_h^{(3),(2)}| \leq \xi |\eta_h|.$$

Then the discretization error estimator η_h is efficient and reliable with the constants $\bar{c}_h = \frac{(1+\xi)}{1-b_h}$ and $\underline{c}_h = \frac{(1-\xi)}{1+b_h}$.

Proof. This proof is also presented in [21]. From the proof Corollary 3.6, we know

$$\frac{1}{1+b_h} |\eta| \leq |J(U) - J(\tilde{U})| \leq \frac{1}{1-b_h} |\eta|.$$

Now we use that $|\eta| = |\eta_h + \eta_k + \mathcal{R}_h^{(3),(2)}|$. From the triangle inequality and the inverse triangle inequality, we get

$$\begin{aligned} |\eta| &\leq |\eta_h| + |\eta_k + \mathcal{R}_h^{(3),(2)}| \leq (1 + \xi) |\eta_h|, \\ |\eta| &\geq |\eta_h| - |\eta_k + \mathcal{R}_h^{(3),(2)}| \geq (1 - \xi) |\eta_h|. \end{aligned}$$

Combining this result with the result from above gives

$$\frac{(1-\xi)}{1+b_h} |\eta_h| \leq |J(U) - J(\tilde{U})| \leq \frac{(1+\xi)}{1-b_h} |\eta_h|.$$

This already proves the result with the constants $\bar{c}_h = \frac{(1+\xi)}{1-b_h}$ and $\underline{c}_h = \frac{(1-\xi)}{1+b_h}$. \square

Remark 3.8. *Using some further estimates from [21] one can show that the effectivity index*

$$I_{eff} := \frac{|\eta_h|}{|J(U) - J(\tilde{U})|} \quad (11)$$

satisfies $I_{eff} \in [\frac{(1-\xi)}{1+b_h}, \frac{(1+\xi)}{1-b_h}]$. Additionally, we define the primal effectivity index

$$I_{eff,p} := \frac{|\eta_p|}{|J(U) - J(\tilde{U})|},$$

and the adjoint effectivity index

$$I_{eff,a} := \frac{|\eta_a|}{|J(U) - J(\tilde{U})|}.$$

We would like to mention that for linear problems $I_{eff,p} = I_{eff,a}$.

Remark 3.9. *In our numerical experiments, we use Newton's method until $|\eta_k| < 10^{-10}$.*

3.2 Multiple goals

In many applications, there are more functionals of interest. For example in the case of our model problem, that could be the temperature at a given point x_{θ_1} ; i.e $J(U) = \theta(x_{\theta_1})$ or the mean magnitude of the velocity of the fluid; i.e $J(U) = \int_{\Omega} |v| dx$. Now let us assume we have $N \in \mathbb{N}$ functional evaluations J_1, \dots, J_N in which we are interested in. One possible way would be to simply add all functionals to one, i.e $J_A := \sum_{i=1}^N J_i$. However, this may lead to error cancellation effects. For instance, let us assume that $N = 3$ and $J_1(U) - J_1(\tilde{U}) = 1$, $J_2(U) - J_2(\tilde{U}) = 1$ and $J_3(U) - J_3(\tilde{U}) = -2$ then $J_A(U) - J_A(\tilde{U}) = 0$. This indicates that the error vanishes, but this is not true for any of the original functionals.

3.2.1 Combined Functional

To overcome the error cancellation effects when combining the functionals, we use a weighted sum with signed weights as done in [32, 31, 27, 20, 23]. The combined functional, which is motivated by [23] is finally given by

$$J_c(v) := \sum_{i=1}^N w_i J_i(v) \quad \text{with} \quad w_i := \omega_i \frac{J(U_h^{(2)}) - J(\tilde{U})}{|J(U_h^{(2)}) - J(\tilde{U})|}, \quad (12)$$

where $w_i = \omega_i C$ with $C \in \mathbb{R}$ if $|J(U_h^{(2)}) - J(\tilde{U})| = 0$. Here, w_i are user chosen weights. In our numerical examples, we set $w_i = |J(\tilde{U})|^{-1}$ for non vanishing functionals and 1 for vanishing functionals. As explained in [23] this choice of w_i leads to a similar relative error in all the functionals. For more details on this combined functional, we refer to [27, 23]. Finally, we can apply the theory from the single case to the combined functional J_c .

3.3 Algorithms

In this subsection, we introduce our three main algorithms, namely line search, the Newton's method, and the final adaptive algorithm.

Algorithm 1 Line search

```

1: procedure LINE SEARCH( $\beta, A, U, P, \text{maxiterL}$ )
2:    $\alpha \leftarrow 1, k \leftarrow 0$ 
3:   while  $\|A(U + \alpha P)\| \geq \|A(U + \alpha P)\|$  &  $k \geq \text{maxiterL}$  do
4:      $\alpha \leftarrow \beta \alpha$ 
5:      $k \leftarrow k + 1$ 
   return  $U + \alpha P$ 

```

Remark 3.10. *In our numerical experiments, we used $\beta = 0.7$ and $\text{maxiterL} = 20$.*

Algorithm 2 Newton' method with line search

```
1: procedure NEWTON'S METHOD( $A, U^0, \text{res}, \text{maxiterN}$ )
2:    $k \leftarrow 0, U^k \leftarrow U^0$ 
3:   while  $\|A(U^k)\| \geq \text{res} \ \& \ k \geq \text{maxiterN}$  do
4:     Solve  $A'(U)(P) = -A(U)$  for  $P$ .
5:      $U^{k+1} \leftarrow \text{Line search}(\beta, A, U^k, P, \text{maxiterL})$ 
6:      $k \leftarrow k + 1$ 
return  $U^k$ 
```

Remark 3.11. *In our numerical experiments we used $\text{res} = \text{maximum}(10^{-12}, 10^{-9}) \|A(U^0)\|$*

Algorithm 3 The adaptive algorithm

```
1: procedure ADAPTIVE ALGORITHM( $J, A, \mathcal{T}_0, \text{TOL}, \text{maxNDoFs}$ )
2:    $k \leftarrow 0, \mathcal{T}_k \leftarrow \mathcal{T}_0, \eta_h \leftarrow \infty$ 
3:   while  $\eta_h > 10^{-2} \text{TOL} \ \& \ |\mathcal{T}_k| \geq \text{maxNDoFs}$  do
4:     Solve (8) and (2) to obtain  $U_h^{(2)}$  and  $U_h$  using Newton's method.
5:     Solve (9) and (3.1) to obtain  $Z_h^{(2)}$  and  $Z_h$  using some linear solver.
6:     Compute  $\eta_h$  and the node-wise error contribution  $\eta_i^{PU}$  as in (10).
7:     Distribute  $\eta_i^{PU}$  equally to all elements that share the node  $i$ .
8:     Mark the elements using some marking strategy.
9:     Refine the mesh
10:     $k \leftarrow k + 1$ 
return  $J(U_h)$ 
```

Remark 3.12. *In Algorithm 3 and 2 the arising linear problems are solved using the direct solver UMFPACK [16].*

Remark 3.13. *In the marking strategy in Algorithm 3, we mark to 10% of all elements, when ordered with respect to their error contribution.*

Remark 3.14. *If $J = J_c$ as defined in (12) then we return all $J_i(U_h)$.*

4 Numerical experiments

In this section, we conduct several numerical experiments in two space dimensions. The programming code is based on the open source library deal.II [5, 4] and our algorithmic framework developed in [23]. In all numerical experiments we use $\rho_0 = 998.21$, $\nu_0 = 2.216065960663198 \times 10^{-6}$ and $E_A = 14906.585117275014$. The thermal conductivity $k = 0.5918$. Furthermore, we combine the single functionals to J_c as defined in (12).

4.1 Prerefinement around laser

In the numerical examples, we approximate a point laser in $y \in \mathbb{R}$ with the Gaussian function

$$f_{E,y}(x) := E \left(\frac{1.0}{\sqrt{2\pi\sigma^2}} \right)^d e^{-\frac{(x-y)^2}{2\sigma^2}},$$

where d is the space dimension, as energy source for the the heat equation. In the numerical experiments, we noticed that for large E and small σ prerefinement around y is required. This is the case since the right hand side is not sufficiently resolved by the grid. In Figure 1, we show the right-hand side for $E = 1$ and $\sigma \in \{10^{-1}, 10^{-2}, 10^{-3}\}$. Even though all sub figures look alike, we would like to mention that we zoom in each time we pick a smaller sigma. Furthermore, the maximum increases for smaller sigma. As a consequence also the solution of the heat equation for a given velocity field v has high derivatives around y . The motivates the choice of a mesh with local refinement around y . We would like to note that without prerefinement, either the right hand side was approximated badly on coarse grids, and on finer grids, Newton's method did not converge.

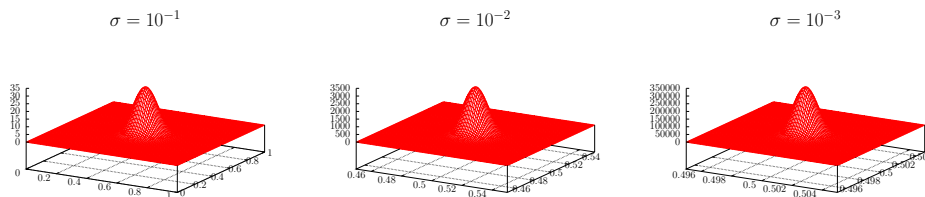


Figure 1: $f_{E,y}(x)$ with $y = \frac{1}{2}(1, 1)$ and $E = 1$ on the domains $[0, 1]^2$ for $\sigma = 10^{-1}$ (left), $[0.45, 0.55]^2$ for $\sigma = 10^{-2}$ (center) and $[0.495, 0.505]^2$ for $\sigma = 10^{-3}$ (right).

4.2 Temperature dependent thermal expansion coefficient

We construct the temperature dependent thermal expansion coefficient $\alpha(\theta)$ using linear splines with the data¹ from Table 1 as support points. Furthermore, we extrapolate $\alpha(\theta)$ in the exterior using the gradient at the boundaries.

4.3 Flow in a square with two lasers

In the first example, there are two lasers in the square $\Omega := (0, 0.3)^2$. We choose $\theta_0 = 293.15$ in (1). The two lasers are represented with a source term, which is modeled by the sum of two Gaussian distributions from above. The

¹[https://www.chemie.de/lexikon/Wasser_\(Stoffdaten\).html](https://www.chemie.de/lexikon/Wasser_(Stoffdaten).html)

temperature in °C	0	4	5	10	15	20	25	30	
$\alpha = 10^{-3} \times$	-0.08	0	0.011	0.087	0.152	0.209	0.259	0.305	
temperature	35	40	45	50	60	70	80	90	99.63
$\alpha = 10^{-3} \times$	0.347	0.386	0.423	0.457	0.522	0.583	0.64	0.696	0.748

Table 1: Thermal expansion coefficient for different temperatures.

centers of the lasers are at $x_1 = (0.05, 0.05)$ and $x_2 = (0.25, 0.05)$, which together with Ω is depicted in the left sub figure of Figure 2. The right hand side function is chosen as

$$f_E(x) := E \left(\frac{1}{\sqrt{2\pi\sigma^2}} \right)^2 e^{-\frac{(x-x_1)^2}{2\sigma^2}} + E \left(\frac{1}{\sqrt{2\pi\sigma^2}} \right)^2 e^{-\frac{(x-x_2)^2}{2\sigma^2}}$$

with $\sigma^{-2} = 500$ and $E = 10^4$.

4.3.1 Goal functionals

We are interested in the following goal functionals:

- the mean value of the magnitude of the velocity:

$$J_1(U) := \frac{1}{|\Omega|} \int_{\Omega} |v| \, dx,$$

- the mean value of the temperature in the domain:

$$J_2(U) := \frac{1}{|\Omega|} \int_{\Omega} \theta \, dx,$$

- the temperature at the center $y = (0.15, 0.15)$ which is shown in Figure 2:

$$J_3(U) := \theta(y).$$

4.3.2 Discussion of our findings

As already mentioned in Subsection 4.1 preresinement at the position of the laser was required in order for the Newton's method to converge and to resolve the right the function f_E . The resulting initial mesh is visualized in Figure 2.

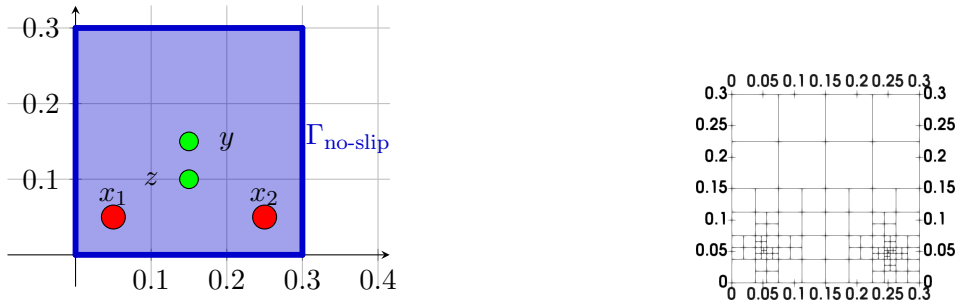


Figure 2: Example 1+2: The domain Ω $\Gamma_{\text{no-slip}}$ and x_1 and x_2 (left) and the initial mesh (right)

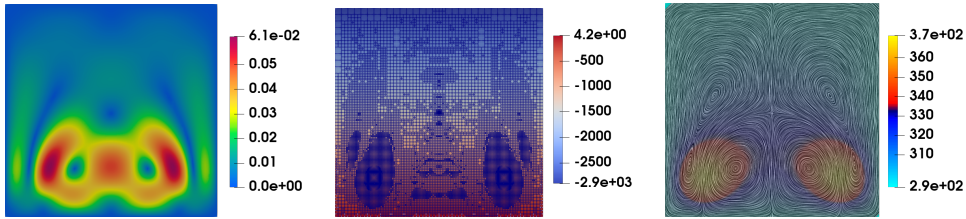


Figure 3: Example 1: Magnitude of velocity(left), pressure and adaptively refined mesh (center) and streamlines and temperature (right)

The numerical results for our first are presented in Figures 3 - 5 on pages 14 - 15. Both the streamlines (right) and the magnitude (left) of the velocity v are shown in Figure 3. Furthermore, there are at least six vortices.

However, refining in the corners of Ω generates more vortices at these corners. The impact of these vortices on our quantities of interest is negligible, since the goal oriented error estimator, would mark those elements for refinement otherwise. In Figure 5, we observe that the error in the combined functional is dominated by J_1 . Therefore, the refinement is primarily driven by the refinement of this quantity of interest, which can be seen in Figure 3. The relative errors of the other quantities of interest are almost one order of magnitude less. This also explains, why there is just a light refinement at y , compared to other examples with point evaluations as quantity of interest; see [19, 44] and other examples in this work. The temperature θ in our computation is between $293.15K$ and $373.15K$ as represented in Figure 3. We would like to mention that on coarse meshes, the effectivity index was between 0.1 and 0.2 on coarse meshes. This is an additional indicator the the function f_E , was not good enough resolved on the initial mesh. This is shown in Figure 4. On finer meshes, we obtain effectivity indices between 0.68 and 0.82.

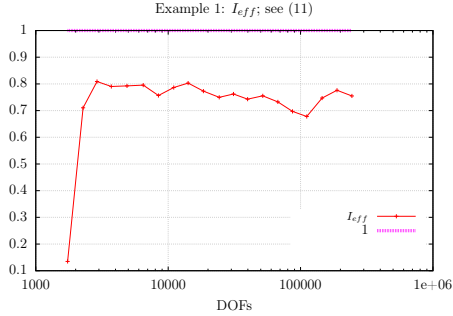


Figure 4: Example 1: Effectivity index.

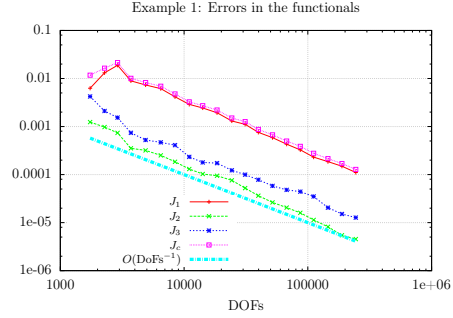


Figure 5: Example 1: Relative errors for J_1 , J_2 , J_3 and absolute error for J_c .

4.4 Flow in a square with two lasers with different focus

In this subsection, we change the focus of the laser, namely the parameter σ . We use

$$\sigma \in \{10^{-1}, 10^{-2}, 10^{-3}, 10^{-4}\}.$$

Furthermore in all examples, we set $E = 100$. All other parameters are the same as in previous example. We have the following quantities of interest:

- the mean value of the magnitude of the velocity:

$$J_1(U) := \frac{1}{|\Omega|} \int_{\Omega} |v| dx,$$

- the mean value of the temperature in the domain:

$$J_2(U) := \frac{1}{|\Omega|} \int_{\Omega} \theta dx,$$

- the temperature at y :

$$J_3(U) := \theta(y),$$

- the temperature at z

$$J_4(U) := \theta(z),$$

where $y = (0.15, 0.15)$ and $z = (0.15, 0.1)$ as visualized in Figure 2, respectively. In our numerical examples we used the following reference values given Table 2.

Reference values	$\sigma = 10^{-1}$	$\sigma = 10^{-2}$	$\sigma = 10^{-3}$	$\sigma = 10^{-4}$
$J_1(U) =$	4.568690×10^{-3}	4.821760×10^{-3}	5.692103×10^{-3}	5.705407×10^{-3}
$J_2(U) =$	299.0619	302.1829	302.3692	302.3710
$J_3(U) =$	305.7956	303.4749	303.4754	303.4754
$J_4(U) =$	306.8565	307.3140	307.3146	307.3146

Table 2: Example 2: reference values

The numerical results for this example are presented in Figures 6 - 17 on pages 18 - 19. For $\sigma = 0.1$, the maximum of the temperature is close to the center, cf. Figure 6. This is in contrast to $\sigma \leq 0.01$, cf. Figures 7 - 9, where the maximum is close to the point sources. This also changes the pattern of the flow, depicted on the right subfigures. Whereas for $\sigma = 10^{-1}$, we just observe two vortices. In Figures 7 to 9, we observe again six for $\sigma = 10^{-2}$, $\sigma = 10^{-3}$ and $\sigma = 10^{-4}$. For $\sigma = 0.1$, cf. Figure 6, the magnitude of the velocity also has its maximum close to the center. Moreover, the gradients of the temperature, and the largest temperature increase for smaller σ as expected. For all σ , the functional J_1 dominates, cf. Figures 14 - 17. Despite of that, the mesh for $\sigma = 10^{-1}$ greatly differs from the others. The adaptively refined meshes of $\sigma = 10^{-2}$, $\sigma = 10^{-3}$ and $\sigma = 10^{-4}$ share many similarities like clover shaped refinement at x_1 and x_2 . Closer inspections also reveals this clover shaped refinement at y and z , which is the typical refinement for point evaluations at this points, i.e. for J_3 and J_4 . This shows that even though J_1 is the dominating, our method provides refinement for the other functionals as well. Furthermore, for the magnitude of velocity on the left of in Figures 6 - 9 increases as σ is decreasing. The effectivity indices are about 0.8 for $\sigma \leq 0.01$, see Figures 11 - 13, if a certain refinement level is reached. For $\sigma = 10^{-4}$ it is very inaccurate for a small amount of DoFs. This is due to the strong point source. The result for $\sigma = 0.1$ is quite different.

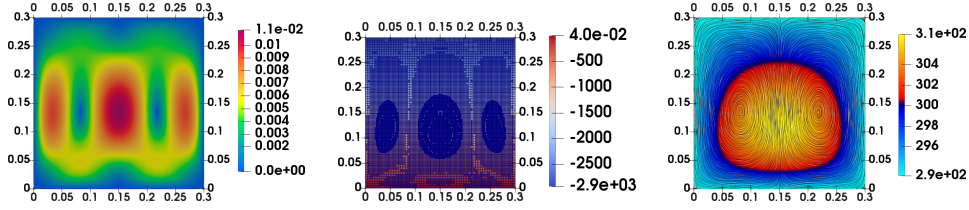


Figure 6: Example 2: Magnitude of velocity v (left), the pressure with the adaptive mesh(center) and temperature and flow field (right) for $\sigma = 10^{-1}$.

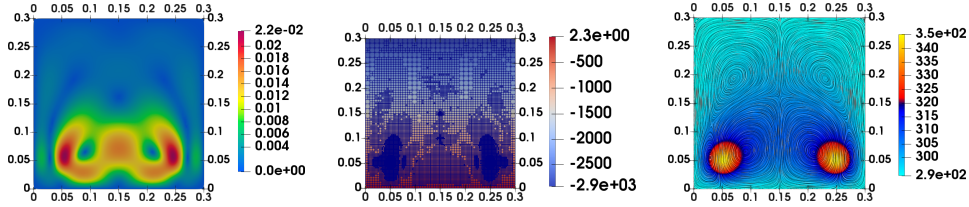


Figure 7: Example 2: Magnitude of velocity v (left), the pressure with the adaptive mesh(center) and temperature and flow field (right) for $\sigma = 10^{-2}$.

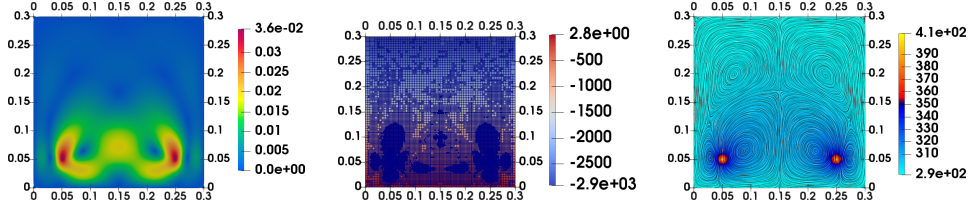


Figure 8: Example 2: Magnitude of velocity v (left), the pressure with the adaptive mesh(center) and temperature and flow field (right) for $\sigma = 10^{-3}$.

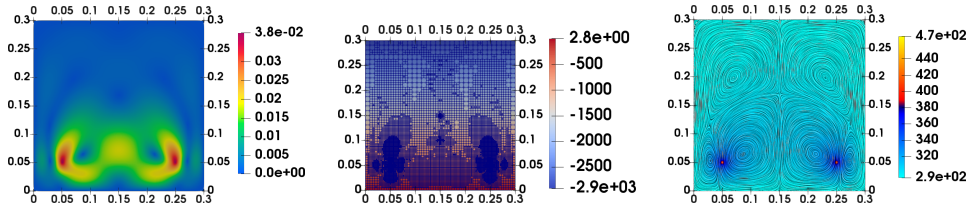


Figure 9: Example 2: Magnitude of velocity v (left), the pressure with the adaptive mesh(center) and temperature and flow field (right) for $\sigma = 10^{-4}$.

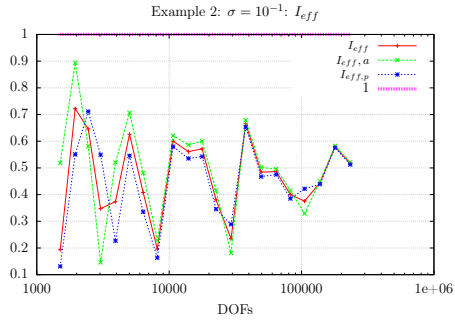


Figure 10: Example 2: Effectivity Indices for $\sigma = 10^{-1}$.

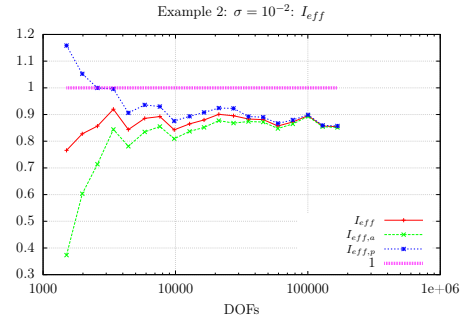


Figure 11: Example 2: Effectivity Indices for $\sigma = 10^{-2}$.

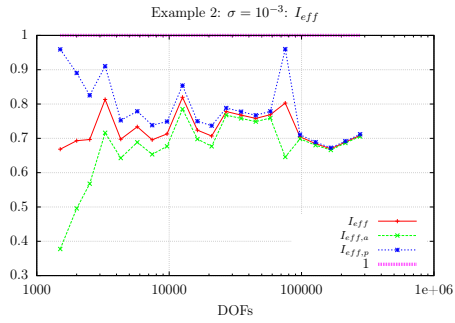


Figure 12: Example 2: Effectivity Indices for $\sigma = 10^{-3}$.

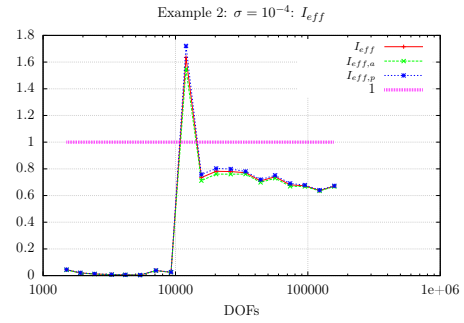


Figure 13: Example 2: Effectivity Indices for $\sigma = 10^{-4}$.

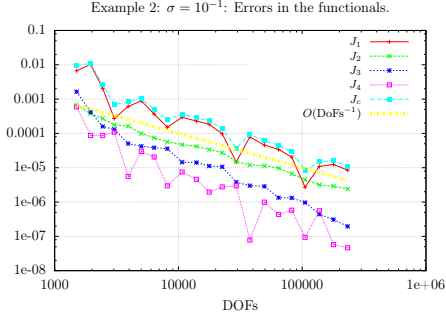


Figure 14: Example 2: Relative errors in J_i , $i \in \{1, 2, 3, 4\}$, and absolute error in J_c for $\sigma = 10^{-1}$.

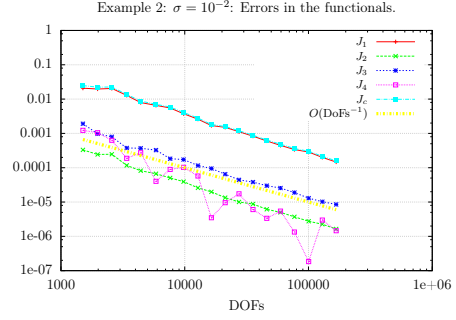


Figure 15: Example 2: Relative errors in J_i , $i \in \{1, 2, 3, 4\}$, and absolute error in J_c for $\sigma = 10^{-2}$.

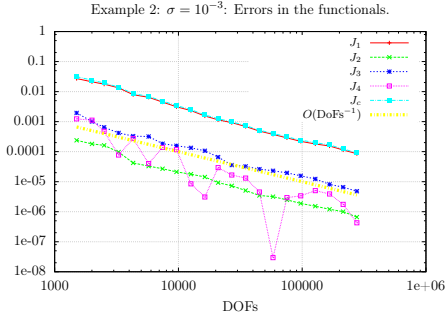


Figure 16: Example 2: Relative errors in J_i , $i \in \{1, 2, 3, 4\}$, and absolute error in J_c for $\sigma = 10^{-3}$.

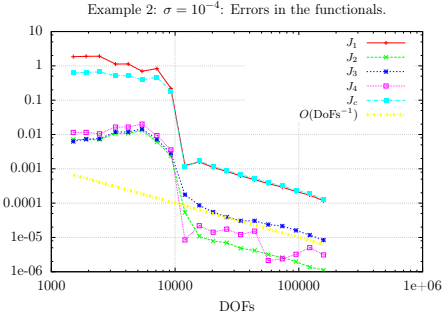


Figure 17: Example 2: Relative errors in J_i , $i \in \{1, 2, 3, 4\}$, and absolute error in J_c for $\sigma = 10^{-4}$.

4.5 Circle with a comparison between density and Boussinesq

In the last example, the computational domain Ω is a circle with radius 0.2 and center $C = (0, 0)$, i.e. $\Omega := \{x \in \mathbb{R}^2 : |x|^2 < 0.04\}$. Additionally, we have two different lasers on the points $L_A := \frac{1}{20}(-1, -2)$ and $L_B := \frac{1}{20}(1, -2)$ with focus $\sigma = 10^{-3}$. These quantities are depicted on Figure 18. We are interested in the following functionals

$$\begin{aligned} J_1(U) &= v_1(L_A), & J_2(U) &= v_2(L_A), \\ J_3(U) &= |v|^2(L_A), & J_4(U) &= p(L_A) - p(L_B), \\ J_5(U) &= \theta(C), & J_6(U) &= \int_{\partial\Omega} \nabla\theta \cdot n ds_x, \end{aligned}$$

where n denotes the outer normal vector. Furthermore, we compare two different models in this example, which is on the one hand our model problem (1). In this example, we use the terminology 'Density', if we refer to

our model problem. In case of the following Boussinesq problem, we use the terminology 'Boussinesq' to refer to this problem.

The Boussinesq problem is a modification of [34, 12] and given by: Find the velocity field v , the pressure p and the temperature θ such that

$$\begin{aligned} -\operatorname{div}(\nu(\theta)\rho(\nabla v + \nabla v^T)) + (\rho v \cdot \nabla)v - \nabla p - g\rho\alpha(\theta)(\theta - 293.15) &= 0, \\ -\operatorname{div}(v) &= 0, \\ -\operatorname{div}(k\nabla\theta) + v \cdot \nabla\theta &= f_E, \\ \nu(\theta) &= \nu_0 e^{\frac{E_A}{R\theta}}. \end{aligned}$$

The boundary conditions for the Density model and Boussinesq are

$$\begin{aligned} v &= 0 && \text{on } \partial\Omega, \\ \theta &= 274.15 && \text{on } \partial\Omega. \end{aligned} \tag{13}$$

Furthermore, for both problems, i.e. the Density model and Boussinesq,

$$f_E := \gamma f_{E,L_A} + \gamma^{-1} f_{E,L_B},$$

with $E = 200$ and $\gamma = 2$. This choice of γ makes the laser pointing at L_A stronger than the one pointing on L_B , see the left picture of Figure 18. The reference values used in the numerical experiments are given in Table 3. The numerical results are presented in Figures 19 - 29 on pages 23 - 25 and Table 4 on page 22. As in the previous examples, the initial mesh has some prerenement around the point sources, see the left picture of Figure 18. Figure 21 depicts the temperature and the streamlines of the flow. There are only minimal differences in the temperature. However, the magnitude of the velocity is larger for the Boussinesq model, see Figure 20. In both cases, there are two vortices, one on the left and one on the right. Whereas the right one looks quite similar in both cases, the right one, see Figure 21, becomes more anisotropic for the Boussinesq model. Also the adaptively refined meshes which are displayed in Figure 19 refine more from the point sources away for the Boussinesq model. Figures 24 and 25 display the errors of the functionals J_i , $i = 1, \dots, 6$. The function J_6 dominates the error in both cases. In comparison to the previous examples, the dominance is not so strong. For coarser meshes, J_4 and in the case of Boussinesq also J_1 are quite large. This is changing with the refinement process. For Boussinesq, then also J_3 will become quite large. This results in a very slow decrease of the functional J_6 in the first refinement steps which is worse than a uniform refinement, cf. Figures 26 and 27, in particular for the density model. However, these figures also show that the adaptive procedure converges with approximately $O(\text{DoFs}^{-1})$, in comparison to $O(\text{DoFs}^{-\frac{1}{2}})$ for uniform refinement. Figures 28 and 29 display the situations for the functional J_4 . This functional is decreased quite rapidly in both cases. Here, both adaptive and uniform

refinement have an error reduction in the order of $O(\text{DoFs}^{-1})$. The effectivity indices, which are presented in Figures 22 and 23 are quite different for both models. The authors observe a effectivity indices greater than one for the Density model. They are about 1.2. The effectivity indices are more away from one for the Boussinesq. Moreover, they are less than one.

reference values	Density	Boussinesq
J_1	-0.12361494	-0.16786688
J_2	0.57190820	0.48240847
J_3	0.34235964	0.26089722
J_4	8.62163631	-73.2536833
J_5	353.526189	353.919688
J_6	-844.882355	-844.882273

Table 3: Example 3: Reference values

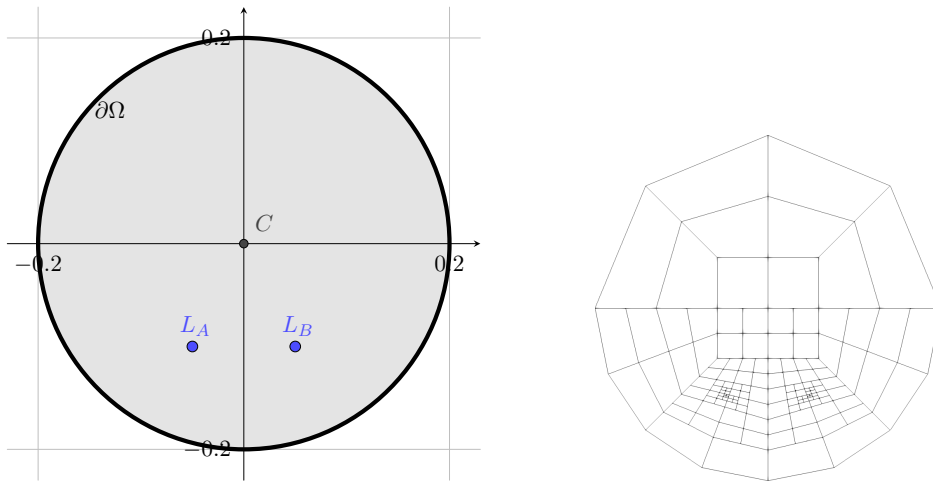


Figure 18: The domain Ω , the center C and the source points of the two lasers L_A and L_B on the left and the initial mesh with prrefinement on L_A and L_B on the right.

# refinements	Density			Boussinesq		
	DoFs	Newton steps	# Linesearch	DoFs	Newton steps	# Linesearch
0	1 680	15	61	1 680	19	88
1	2 458	4	0	2 420	6	0
2	3 216	4	0	3 114	7	0
3	4 428	4	0	4 066	7	0
4	5 982	3	0	5 224	7	0
5	7 940	4	0	6 936	6	0
6	10 404	3	0	9 312	6	0
7	13 532	3	0	12 240	7	0
8	17 636	3	0	15 932	6	0
9	23 032	3	0	21 132	5	0
10	29 862	3	0	27 958	6	0
11	38 774	3	0	36 486	5	0
12	50 320	3	0	47 652	6	0
13	65 480	3	0	61 512	5	0
14	84 822	3	0	80 472	5	0
15	110 122	3	0	105 170	5	0
16	143 414	3	0	137 784	5	0
17	186 514	3	0	182 182	5	0
18	243 002	3	0	236 512	4	0
19	315 344	3	0	309 694	5	0
20	409 738	2	0	406 702	5	0

Table 4: Comparison of required number of Newton and line search steps for the two different models: # refinements denotes the current refinement level, DoFs denotes the number of degrees of freedom, Newton steps the number of Newton steps, # Linesearch denotes the total number of line searches steps required on the current refinement level

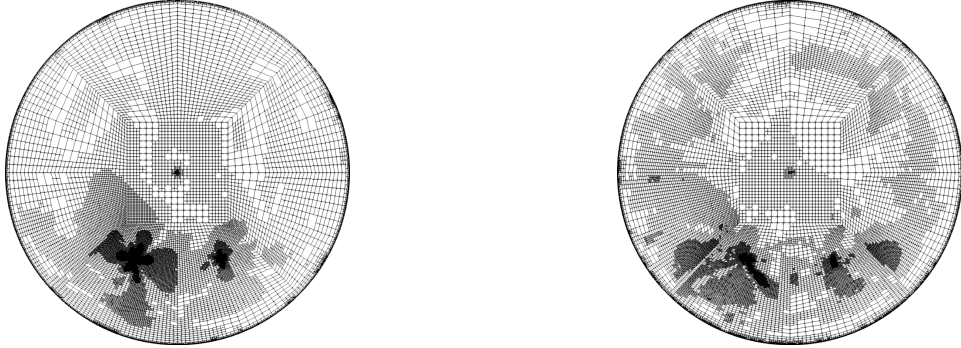


Figure 19: Example 3: Adaptively refined meshes for Density(left) and Boussinesq (right).

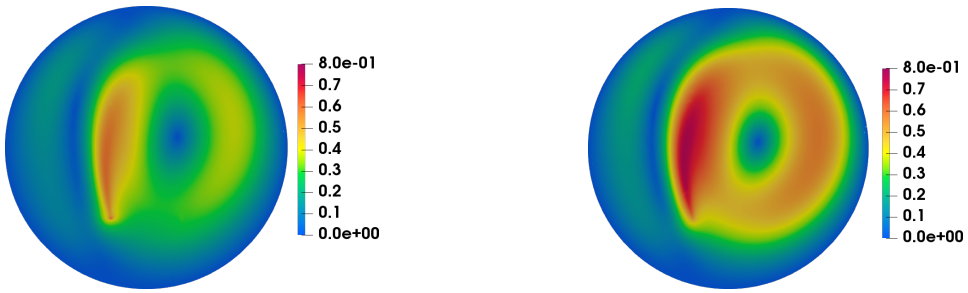


Figure 20: Example 3: Magnitude of the velocity for Density(left) and Boussinesq (right).

Both models are highly nonlinear and solved with Newton's method including line search. The required iteration numbers are displayed in Table 4. Only in the first refinement step, a line search is required. In all other refinement steps a few Newton iterations are necessary until the method is converging. There are about three for the Density model and mostly five or six for the Boussinesq model.

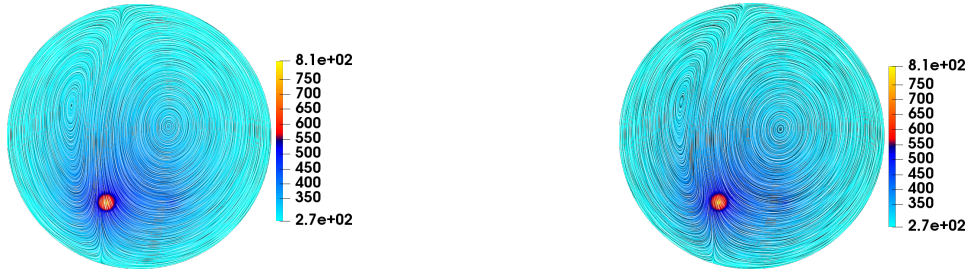


Figure 21: Example 3: Streamlines of the flow and temperature for Density(left) and Boussinesq (right).

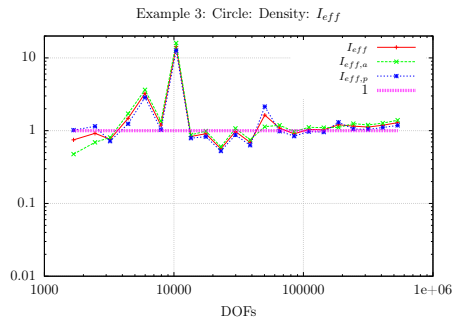


Figure 22: Example 3: Effectivity Indices for Density.

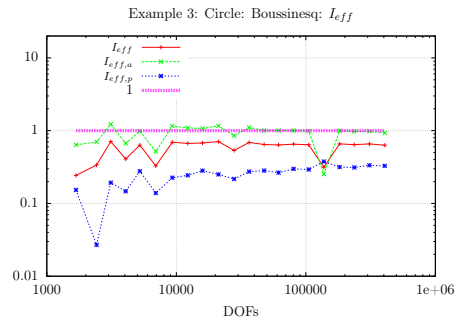


Figure 23: Example 3: Effectivity Indices for Boussinesq.

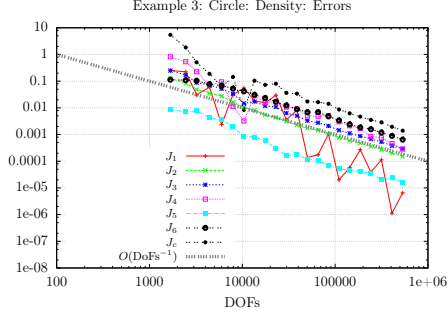


Figure 24: Example 3: Relative errors in J_i , $i = 1, \dots, 6$, and absolute error in J_c for Density.

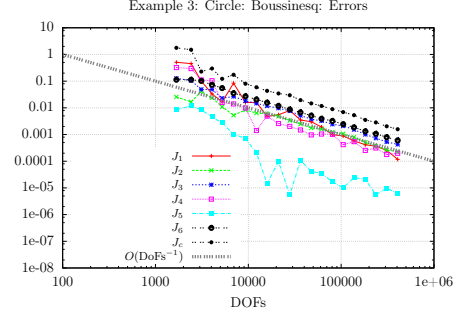


Figure 25: Example 3: Relative errors in J_i , $i = 1, \dots, 6$, and absolute error in J_c for Boussinesq.

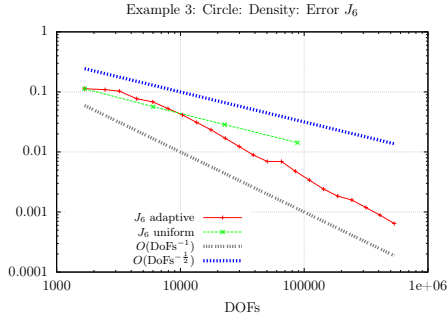


Figure 26: Example 3: Relative errors in J_6 using adaptive and uniform(global) refinement for Density.

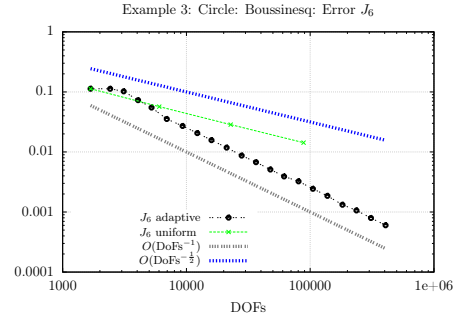


Figure 27: Example 3: Relative errors in J_6 using adaptive and uniform(global) refinement for Boussinesq.

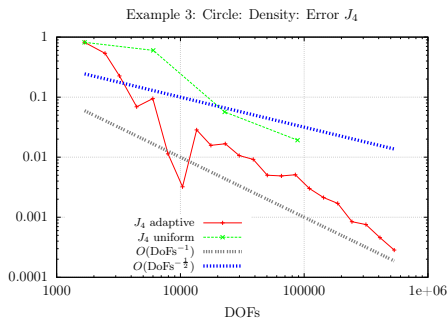


Figure 28: Example 3: Relative errors in J_4 using adaptive and uniform(global) refinement for Density.

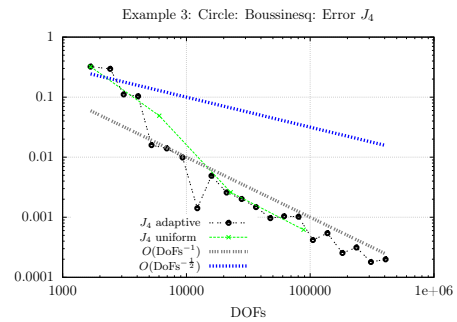


Figure 29: Example 3: Relative errors in J_4 using adaptive and uniform(global) refinement for Boussinesq.

5 Conclusions

In this work, we first proposed a model for coupling the Navier-Stokes equations with a temperature equation in which the density and viscosity both are temperature-dependent. This results into a highly nonlinear problem. We formulated a monolithic setting and applied multigoal-oriented a posteriori error estimation up to six goal functionals (quantities of interest). Therein, adjoint sensitivities measures for the error estimator are obtained with the help of the dual-weighted residual method. Then, motivated from laser material processing, we conducted three numerical tests. Therein, due to the highly nonlinear behavior, our Newton solver would only work with a priori local mesh refinement in certain regions of interest. Moreover, we investigated error reductions and effectivity indices. According to the highly nonlinear behavior and various parameters variations, we obtained satisfying results for both error reductions and effectivity indices.

Acknowledgments

This work has been supported by the Cluster of Excellence PhoenixD (EXC 2122, Project ID 390833453). Furthermore, Bernhard Endtmayer is funded by an Humboldt Postdoctoral Fellowship and greatly acknowledges this. Thomas Wick thanks Šárka Nečasová (Czech Academy of Sciences) for discussions in the course of this work on the Navier-Stokes equations with material dependent coefficients.

References

- [1] K. Ahuja, B. Endtmayer, M. Steinbach, and T. Wick. Multigoal-oriented error estimation and mesh adaptivity for fluid–structure interaction. *Journal of Computational and Applied Mathematics*, 412:114315, 2022.
- [2] M. Ainsworth and J. T. Oden. *A Posteriori Error Estimation in Finite Element Analysis*. Pure and Applied Mathematics (New York). Wiley-Interscience [John Wiley & Sons], New York, 2000.
- [3] E. d. C. Andrade. LVIII. A theory of the viscosity of liquids.—Part II. *The London, Edinburgh, and Dublin Philosophical Magazine and Journal of Science*, 17(113):698–732, 1934.
- [4] D. Arndt, W. Bangerth, T. C. Clevenger, D. Davydov, M. Fehling, D. Garcia-Sanchez, G. Harper, T. Heister, L. Heltai, M. Kronbichler, R. M. Kynch, M. Maier, J.-P. Pelteret, B. Turcksin, and D. Wells. The deal.II library, version 9.1. *Journal of Numerical Mathematics*, 27:203–213, 2019.

- [5] D. Arndt, W. Bangerth, D. Davydov, T. Heister, L. Heltai, M. Kronbichler, M. Maier, J.-P. Pelteret, B. Turcksin, and D. Wells. The deal.ii finite element library: Design, features, and insights. *Computers & Mathematics with Applications*, 2020.
- [6] S. Arrhenius. Über die Dissociationswärme und den Einfluss der Temperatur auf den Dissociationsgrad der Elektrolyte. *Zeitschrift für Physikalische Chemie*, 4U(1):96–116, 1889.
- [7] S. Arrhenius. Über die Reaktionsgeschwindigkeit bei der Inversion von Rohrzucker durch Säuren. *Zeitschrift für Physikalische Chemie*, 4U(1):226–248, 1889.
- [8] W. Bangerth and R. Rannacher. *Adaptive Finite Element Methods for Differential Equations*. Birkhäuser, Lectures in Mathematics, ETH Zürich, 2003.
- [9] M. Bause, M. P. Bruchhäuser, and U. Köcher. Flexible goal-oriented adaptivity for higher-order space–time discretizations of transport problems with coupled flow. *Computers & Mathematics with Applications*, 91:17–35, 2021.
- [10] R. Becker and R. Rannacher. A feed-back approach to error control in finite element methods: basic analysis and examples. *East-West J. Numer. Math.*, 4:237–264, 1996.
- [11] R. Becker and R. Rannacher. An optimal control approach to a posteriori error estimation in finite element methods. *Acta Numerica*, Cambridge University Press, pages 1–102, 2001.
- [12] S. Beuchler, B. Endtmayer, J. Lankeit, and T. Wick. Multigoal-oriented a posteriori error control for heated material processing using a generalized Boussinesq model. *Comptes Rendus. Mécanique*, 2023. Online first.
- [13] I. Brevis, I. Muga, and K. G. van der Zee. A machine-learning minimal-residual (ml-mres) framework for goal-oriented finite element discretizations. *Computers & Mathematics with Applications*, 95:186–199, 2021. Recent Advances in Least-Squares and Discontinuous Petrov–Galerkin Finite Element Methods.
- [14] M. P. Bruchhäuser, K. Schwegler, and M. Bause. Dual weighted residual based error control for nonstationary convection-dominated equations: potential or ballast? In *Boundary and Interior Layers, Computational and Asymptotic Methods BAIL 2018*, pages 1–17. Springer, 2020.

- [15] G. Y. Chen, F. Piantedosi, D. Otten, Y. Q. Kang, W. Q. Zhang, X. Zhou, T. M. Monro, and D. G. Lancaster. Femtosecond-laser-written microstructured waveguides in bk7 glass. *Scientific Reports*, 8(1), 2018.
- [16] T. A. Davis. Algorithm 832: Umfpack v4.3—an unsymmetric-pattern multifrontal method. *ACM Trans. Math. Softw.*, 30(2):196–199, jun 2004.
- [17] J. De Guzman. Relation between fluidity and heat of fusion. *Anales Soc. Espan. Fis. Y. Quim*, 11:353–362, 1913.
- [18] L. Dubrovinsky. Thermal expansion and equation of state. In K. J. Buschow, R. W. Cahn, M. C. Flemings, B. Ilshner, E. J. Kramer, S. Mahajan, and P. Veyssi ere, editors, *Encyclopedia of Materials: Science and Technology*, pages 1–4. Elsevier, Oxford, 2002.
- [19] B. Endtmayer. *Multi-goal oriented a posteriori error estimates for non-linear partial differential equations*. PhD thesis, Johannes Kepler University Linz, 2021.
- [20] B. Endtmayer, U. Langer, I. Neitzel, T. Wick, and W. Wollner. Multigoal-oriented optimal control problems with nonlinear PDE constraints. *Computers & Mathematics with Applications*, 2020.
- [21] B. Endtmayer, U. Langer, T. Richter, A. Schafelner, and T. Wick. *A posteriori single- and multi-goal error control and adaptivity for partial differential equations*. Elsevier, 2024.
- [22] B. Endtmayer, U. Langer, J. Thiele, and T. Wick. Hierarchical DWR Error Estimates for the Navier-Stokes Equations: h and p Enrichment. In *Numerical Mathematics and Advanced Applications ENUMATH 2019*, pages 363–372. Springer, 2021.
- [23] B. Endtmayer, U. Langer, and T. Wick. Multigoal-oriented error estimates for non-linear problems. *J. Numer. Math.*, 27(4):215–236, 2019.
- [24] B. Endtmayer, U. Langer, and T. Wick. Two-Side a Posteriori Error Estimates for the Dual-Weighted Residual Method. *SIAM J. Sci. Comput.*, 42(1):A371–A394, 2020.
- [25] B. Endtmayer, U. Langer, and T. Wick. Reliability and efficiency of dwr-type a posteriori error estimates with smart sensitivity weight recovering. *Computational Methods in Applied Mathematics*, 21(2), 2021.
- [26] B. Endtmayer, A. Schafelner, and U. Langer. Goal-Oriented Adaptive Space-Time Finite Element Methods for Regularized Parabolic p-Laplace Problems. *arXiv preprint arXiv:2306.07167*, 2023.

- [27] B. Endtmayer and T. Wick. A partition-of-unity dual-weighted residual approach for multi-objective goal functional error estimation applied to elliptic problems. *Computational Methods in Applied Mathematics*, 17(2):575–599, 2017.
- [28] E. Feireisl and J. Malek. On the navier-stokes equations with temperature-dependent transport coefficients. *International Journal of Differential Equations*, 2006, 2006.
- [29] E. Fernández Cara. Motivation, analysis and control of the variable density navier-stokes equations. *Discrete and continuous dynamical systems. Series S*, 5 (6), 1021-1090., 2012.
- [30] R. B. Haj-Kacem, N. Ouerfelli, J. Herráez, M. Guettari, H. Hamda, and M. Dallel. Contribution to modeling the viscosity arrhenius-type equation for some solvents by statistical correlations analysis. *Fluid Phase Equilibria*, 383:11–20, 2014.
- [31] R. Hartmann. Multitarget error estimation and adaptivity in aerodynamic flow simulations. *SIAM J. Sci. Comput.*, 31(1):708–731, 2008.
- [32] R. Hartmann and P. Houston. Goal-oriented a posteriori error estimation for multiple target functionals. In *Hyperbolic problems: theory, numerics, applications*, pages 579–588. Springer, Berlin, 2003.
- [33] J. Jacquemin, P. Husson, A. A. H. Padua, and V. Majer. Density and viscosity of several pure and water-saturated ionic liquids. *Green Chem.*, 8:172–180, 2006.
- [34] S. A. Lorca and J. L. Boldrini. Stationary Solutions for Generalized Boussinesq Models. *Journal of Differential Equations*, 124(2):389–406, 1996.
- [35] E. Mallea-Zepeda, E. Lenes, and J. Rodríguez Zambrano. Bilinear optimal control problem for the stationary navier–stokes equations with variable density and slip boundary condition. *Bulletin of the Brazilian Mathematical Society, New Series*, 50:871–887, 2019.
- [36] J. T. Oden. Adaptive multiscale predictive modelling. *Acta Numerica*, 27:353–450, 2018.
- [37] A. Otto and M. Schmidt. Towards a universal numerical simulation model for laser material processing. *Physics Procedia*, 5:35–46, 2010. Laser Assisted Net Shape Engineering 6, Proceedings of the LANE 2010, Part 1.
- [38] X. H. Owe Axelsson and M. Neytcheva. Numerical solution of the time-dependent navier–stokes equation for variable density–variable viscosity. part i. *Mathematical Modelling and Analysis*, 20(2):232–260, 2015.

- [39] D. Pardo. Multigoal-oriented adaptivity for hp-finite element methods. *Procedia Computer Science*, 1(1):1953–1961, 2010.
- [40] W. M. Pätzold, A. Demircan, and U. Morgner. Low-loss curved waveguides in polymers written with a femtosecond laser. *Opt. Express*, 25(1):263–270, Jan 2017.
- [41] J. Pech. Scheme for evolutionary navier-stokes-fourier system with temperature dependent material properties based on spectral/hp elements. In S. J. Sherwin, D. Moxey, J. Peiró, P. E. Vincent, and C. Schwab, editors, *Spectral and High Order Methods for Partial Differential Equations ICOSAHOM 2018*, pages 465–475, Cham, 2020. Springer International Publishing.
- [42] C. Raman. A theory of the viscosity of liquids. *Nature*, 111(2790):532–533, 1923.
- [43] R. Rannacher and J. Vihharev. Adaptive finite element analysis of nonlinear problems: balancing of discretization and iteration errors. *Journal of Numerical Mathematics*, 21(1):23–61, 2013.
- [44] T. Richter and T. Wick. Variational localizations of the dual weighted residual estimator. *Journal of Computational and Applied Mathematics*, 279(0):192 – 208, 2015.
- [45] E. H. van Brummelen, S. Zhuk, and G. J. van Zwieten. Worst-case multi-objective error estimation and adaptivity. *Comput. Methods Appl. Mech. Engrg.*, 313:723–743, 2017.
- [46] K. van der Zee, E. van Brummelen, I. Akkerman, and R. de Borst. Goal-oriented error estimation and adaptivity for fluid–structure interaction using exact linearized adjoints. *Computer Methods in Applied Mechanics and Engineering*, 200(37):2738–2757, 2011. Special Issue on Modeling Error Estimation and Adaptive Modeling.
- [47] A. Ward. The viscosity of pure liquids. *Transactions of the Faraday Society*, 33:88–97, 1937.
- [48] R. K. Zeytounian. Joseph Boussinesq and his approximation: a contemporary view. *Comptes Rendus Mecanique*, 331(8):575–586, 2003.